Available on CMS information server

**CMS NOTE AN-2006/100**

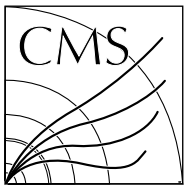

**The Compact Muon Solenoid Experiment**

**CMS Note**

Mailing address: CMS CERN, CH-1211 GENEVA 23, Switzerland

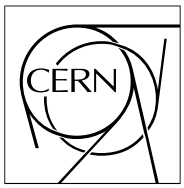

**September 11, 2006**

# Reconstruction of low $p_T$ charged particles with the pixel detector

Ferenc Siklér

*KFKI Research Institute for Particle and Nuclear Physics, Budapest, Hungary*

**Abstract**

With modified hit triplet finding the pixel detector can be employed for the reconstruction of low $p_T$ charged particles. The acceptance of the method extends down to 0.1, 0.2 and 0.3 GeV/$c$ in $p_T$ for pions, kaons and protons, respectively. The fake rate can be greatly reduced, and kept at or below the percent level, with help of information present in the shape of the pixel cluster. Acceptance and efficiency of 80-90% can be achieved, with $p_T$ resolution of 5.5% in the central region.

# 1 Introduction

The reconstruction of low $p_T$ charged particles is crucial for hadron physics where the measured particle yields, spectra and correlations have to be compared to model predictions [1]. The physics of rare high $p_T$ events also needs good knowledge about the characteristics of the underlying background collisions. It is important for high energy physics in general.

In the CMS detector the high occupancy of silicon strips in central A+A collisions makes their inclusion into charged particle tracking difficult [2]. The use of silicon pixels alone allows to use the same analysis for low multiplicity p+p, p+A and high multiplicity A+A events. At the same time this choice enables the reconstruction of very low $p_T$ particles, even down to 0.1 GeV/$c$ for pions, with low fake rate.

In collision of hadrons and nuclei the most abundantly produced charged particles are pions, kaons and protons of both charges. Secondary electrons and positrons are also created by photon conversion in materials (beam-pipe, silicon layers and support). For this reason the demonstration plots in this note show measured quantities for the three long-lived charged particles: pions, kaons and protons. (The identification of these particles is indeed possible. The specific energy loss can be extracted using the energy deposited in the detector, both truncated mean and maximum likelihood methods are applicable.)

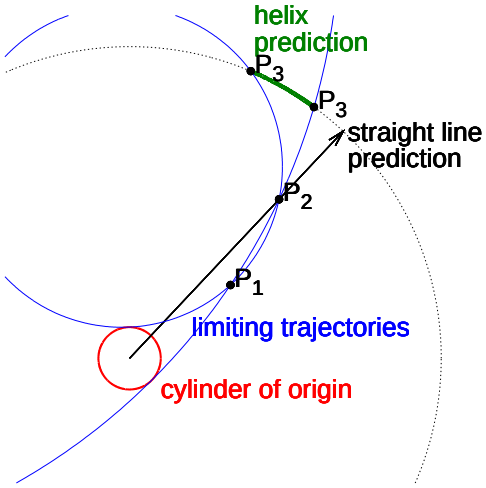


Figure 1: Schematic comparison of the standard straight line prediction and the new helix prediction for finding the third hit. Limiting trajectories (solid blue) that touch the cylinder of origin cut out an arc (thick green) from the barrel layer of the third hit candidates. In the standard method the azimuth of the outer hit $P_2$ is used (solid black arrow).

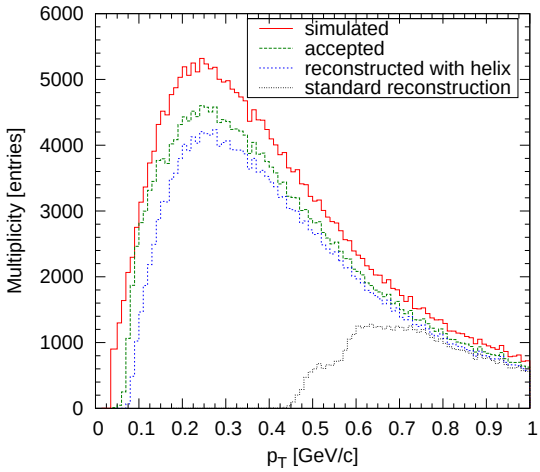


Figure 2: Transverse momentum distribution of simulated (solid red), accepted (green dashed) and reconstructed charged particles. For comparison the result of the new helix method (dotted blue) and the standard one (dotted black) is given. The definitions are given in Section 4.

# 2 Modified hit triplet finding

The standard pixel hit triplet algorithm [3] first finds hit pairs, then for each pair it predicts the range of possible coordinates ($\phi$ and $z$ or $r$) of the third hit. The method uses a straight line through the inner hit and outer hit of the pair in order to get the $z/r$ prediction. The $\phi$ prediction is simply the corresponding value of the outer hit (Fig. 1). Tolerances are set such that they take into account the effects of multiple scattering. When going to lower $p_T$, the nature of the prediction sets back the reconstruction of particles increasingly below $p_T \approx 0.9$ GeV/$c$, even disables it for $p_T < 0.5$ GeV/$c$ (Fig. 2).

Low $p_T$ particles can only be found if the search for the third hit is modified, keeping the logic of track finding intact. Hit pairs are formed first, $P_1$ and $P_2$ are chosen from different pixel layers. During the search for the third hit $P_3$ the following requirements must be fulfilled:

- "origin": the track must come from the cylinder of origin. The cylinder is given by its radius, half-length and position along the beam-line.
- "minimum": the $p_T$ of the track must be above the minimal value $p_{T,min}$.
- "third": the track must be able to reach the layer (barrel or endcap) where the candidates for the third hit are located.

## 2.1 Limiting circles, allowed ranges

In the small volume of the pixel detector the magnetic field is practically constant, the charged particles propagate on helices. The projection of a helix or a cylinder onto the transverse plane is a circle. With a given cylinder of origin and a point pair $P_1$ and $P_2$ each requirement defines a region of allowed track trajectories. Each region is enclosed by a pair of so called limiting circles, projection of extreme trajectories. The "allowed" tracks pass though both $P_1$ and $P_2$ and they locate in the intersection of these regions. The task is to construct the limiting circles. The detailed geometrical discussion in Section A.1 shows that it can be done using an inversion with center $P_1$ and radius $P_1P_2$.

With help of the $z$ coordinates of points $P_1$ and $P_2$, any allowed circle can be transformed back to a helix (see Section A.2). The third hit candidates are located on a layer. The thrusts of allowed helices on the surface of that layer form a curve. It is not necessarily a line, but already well approximated by a parabola in proper coordinates: $(\phi, z)$ for barrel and $(\phi, r)$ for endcap. A parabola can be defined from three points, hence three special trajectories are needed: the two limiting helices and a central helix. The hit cache providing the third hit candidates expects ranges in $(\phi, z/r)$ coordinates. In order to match that, the rectangular envelope of the corresponding part of the parabola is calculated.

A slow particle can be deflected by multiple scattering. In order not to lose hit candidates the envelopes have to be broadened, tolerances should be set. The deduced acceptance of the pixel detector for this method is given in Section 4.1. The lower limits in $p_T$ are 0.1, 0.2 and 0.3 GeV/$c$ for pions, kaons and protons, respectively. At these momenta the standard deviation of the multiple scattering distribution is similar for all the three particle types. It is about 0.02 rad if the thickness of the material is 1% radiation length. Simple calculation leads to tolerances in $\phi$ (0.03 rad) and in $z/r$ (0.3 cm).

## 2.2 Third hit candidates

The provided third hit candidates are examined next. The combination of the point pair $P_1$ and $P_2$ with a candidate $P_3$ defines unambiguously a circle in the transverse plane. The helix has a linear relationship between the azimuthal angle with respect to the center of the circle and the $z$ coordinate. This way, with help of the positions of $P_1$ and $P_2$, the $z$ coordinate of the third hit $P_3$ can be predicted. The measured $z$ coordinate differs from the prediction mainly due to multiple scattering in the intermediate pixel layers and support. In the low momentum range multiple scattering is proportional to $1/(\beta p)$ which is roughly inversely proportional to the mass of the particle. Hence protons scatter more than kaons, kaons scatter more than pions. The amount of multiple scattering, its standard deviation $\sigma$ for relativistic particles ($\beta = 1$), can be obtained from parametrisation (see Appendix of [3]). For the calculation of $\sigma$, the position of $P_2$ together with the parameters $(\eta, p_T)$ of the track candidate have to be provided ("one point constraint"). In $z$ direction, for low momentum

$$\sigma_z(\theta, \beta) = \frac{\sigma}{\beta \sin\theta} \tag{1}$$

At this stage of the reconstruction the type of the particle is not known yet. Therefore, the mass of the mostly produced particle, the pion, is assumed for the calculation of $\beta$. The amount of multiple scattering can be studied in detail by plotting the difference of the measured and predicted $z$ coordinates of the third hit candidates, in units of $\sigma_z$ (Fig. 3). Departures are clearly present for barrel layers where the distributions are wider than expected: 20% increase for kaons and 40% for protons. This can be explained by the fact that the calculation of $\beta$ with the false mass affects low momentum particles and these are less abundant in the endcap layers. Taking this observation into account, a candidate $P_3$ is accepted if its $z$ position is closer to the prediction than $4\sigma_z$.

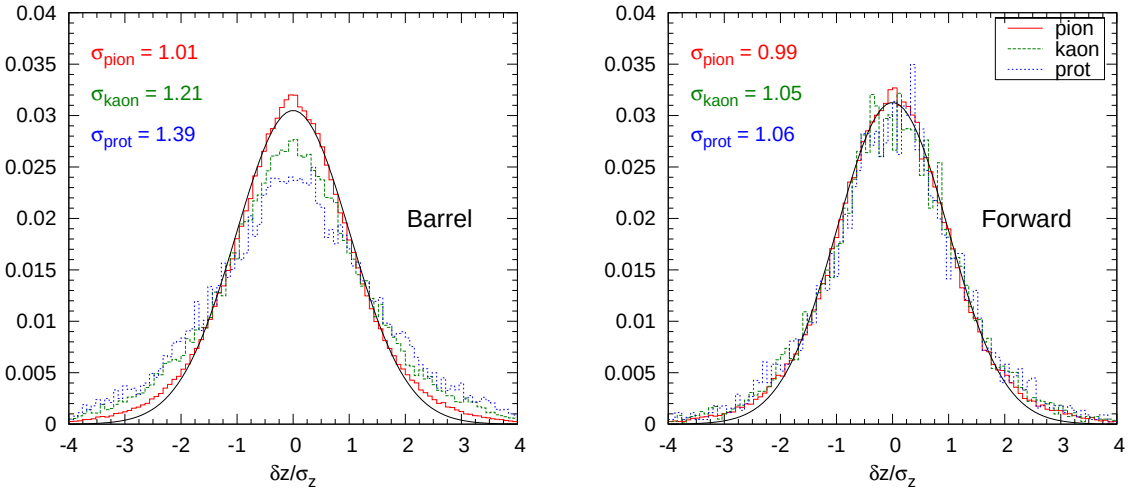


Figure 3: Study of multiple scattering connected to third hit candidates on barrel layers (left) and endcap layers (right). $\delta z$ is the difference between the measured and the predicted $z$ position of the hit, $\sigma_z$ is the standard deviation of the $\delta z$ distribution expected from multiple scattering parametrisation, assuming pion mass. Distribution of ratios $\delta z/\sigma_z$ is shown for pions (solid red), kaons (green dashed) and protons (blue dotted). Results of Gaussian fits for the different particle types are given, the fit curve for pions is shown (black solid).

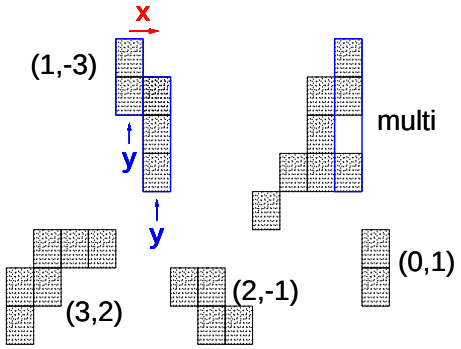


Figure 4: Directed envelopes. The sample cluster at the top left corner consists of two vertical columns (blue rectangles) marked by vertical arrows in $y$ direction (blue arrows). The comparison of the columns proceeds in $x$ direction (red arrow). The resulted signed dimensions of the envelopes are given in parentheses. The cluster labelled "multi" is not compatible with a single particle hit because its rightmost column has an empty pixel .

# 3 Triplet cleaning

While high $p_T$ tracks are relatively clean, pixel hits can often be combined to form fake low $p_T$ tracks. It is therefore important to filter out this undesirable background. This can be achieved using the information present in the shape of the pixel cluster and by looking at lost hits.

**Cluster shape information.** A hit contains much more information than merely its position. An incoming charged particle leaves energy, charge in the pixels. Neighboring pixels (those with common edge or vertex) are grouped to form a cluster, a reconstructed hit. The size, elongation, of the cluster will depend on the angle of incidence of the particle: bigger angles will result in longer clusters. This observation can be exploited in many ways. Among others it can be used to check whether the measured shape of the cluster is compatible with the predicted angle of incidence of the track.

A pixel cluster can be described by the dimension of its directed "envelope". First, the cluster is decomposed into a set of columns covering the pixels in local $y$ direction (see Fig. 4). Each column has a minimal and a maximal $y$ position. The relative positions of the columns are compared successively starting from the first column with the lowest local $x$ position. If the minimal and maximal $y$ position of the second column changes properly with respect to the first one, the cluster will have a trend in $y$. If the maximum and/or the minimum increases the trend is positive, while in case of a decrease it is negative. If the maximum and the minimum move in opposite directions or if there are empty pixels in the column, the cluster is not compatible with a single particle hit. The comparison continues until the column with highest $x$ position is processed. The envelope of the cluster has a definite direction if the trend did not change during the comparison of columns. The dimension $(\Delta x_{meas}, \Delta y_{meas})$ of the directed envelope is simply the size of envelope in pitch units, but its size in $y$ is multiplied by the trend (+1 or -1). Some

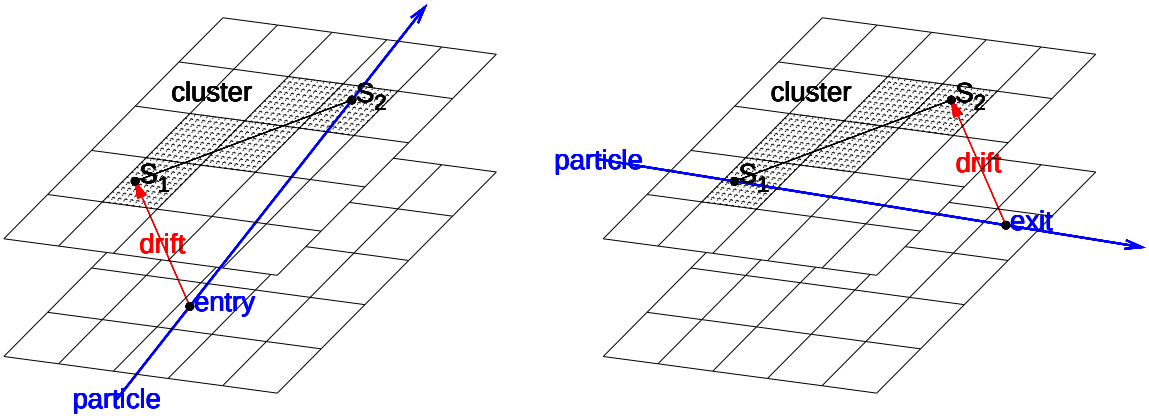


Figure 5: Effect of the Lorentz-shift. A charged particle (blue) crosses the pixel layer. The produced electrons drift (red) towards the pixels of the upper readout plane, hence the charge appears on the line segment $S_1S_2$. The particle can come from below (left) or from above (right), still giving the same line segment and thus the same cluster shape. This explains the fact that for a given cluster envelope there are always two corresponding possible particle directions.

examples are given in Fig. 4. (The cluster might also be skipped if it is at the boundary of a silicon unit.)

A particle crossing is defined by its entry and exit points. The "movement" vector in local coordinates is given by the pair $(\Delta x_{real}, \Delta y_{real})$ which is the planar projection of the vector connecting the entry and exit points (see Fig. 5). Due to the effect of the crossed electric and magnetic fields the drift direction is not normal to the surface but rotated in $x$ direction. This way the vector $S_1\vec{S}_2$ of the drifted charge (on the readout plane) will differ from the movement vector. The particle can come from below or from above, still giving the same line segment and thus the same cluster shape. Hence for a given envelope there are always two corresponding possible particle directions and movements.

The connection between the envelope and the movement was obtained from fast simulation. 10 million minimum ionising (388 eV/$\mu$m) particles with flat movement distribution were generated. The energy deposits were collected in the pixels of a model silicon unit (pitches of 155 $\mu$m and 101 $\mu$m; thickness of 300 $\mu$m). A pixel was filled if the deposited energy reached the threshold value of 5 times the standard deviation of the electric noise ($5 \cdot 3.7 = 18.5$ ADC). After digitisation and clusterization the directed envelope was determined and the movement vector was stored. For a given envelope the compatible movements form two distinct groups (Fig. 6 top). In each group the points have triangular distribution both in $\Delta x_{real}$ and in $\Delta y_{real}$. Therefore the entries can be enclosed by two boxes, a Gaussian fit is not justified. Separate tables have been produced for barrel and endcap layers because they have different Lorentz-shifts (127 $\mu$m and $-43$ $\mu$m in $x$ direction, respectively).

In reality the energy deposits are not simply proportional to the path-lengths but largely fluctuate. In order to compensate for this difference, the boxes have been widened by 0.2 units. The results have been cross-checked with detailed Geant simulation (Fig. 6 bottom). It is clear that the different compatibility boxes contain almost every produced entries.

**Lost hits.** In the endcap layers the particles have small angle of incidence. Hence the compatibility check with the shape of the pixel cluster is less efficient than in case of barrel layers. This results in higher fake rate and higher fraction of multiple counted tracks. The situation can be improved if the tracks are checked for lost hits. In this note a very simple solution is used: only special triplets are allowed. Namely, the first two hits must lie on the two inner barrels, while the third hit can be on the outer barrel or on one of the closer endcaps.

The constructed hit triplets, pixel tracks, can be already passed to the usual momentum fitting procedure.

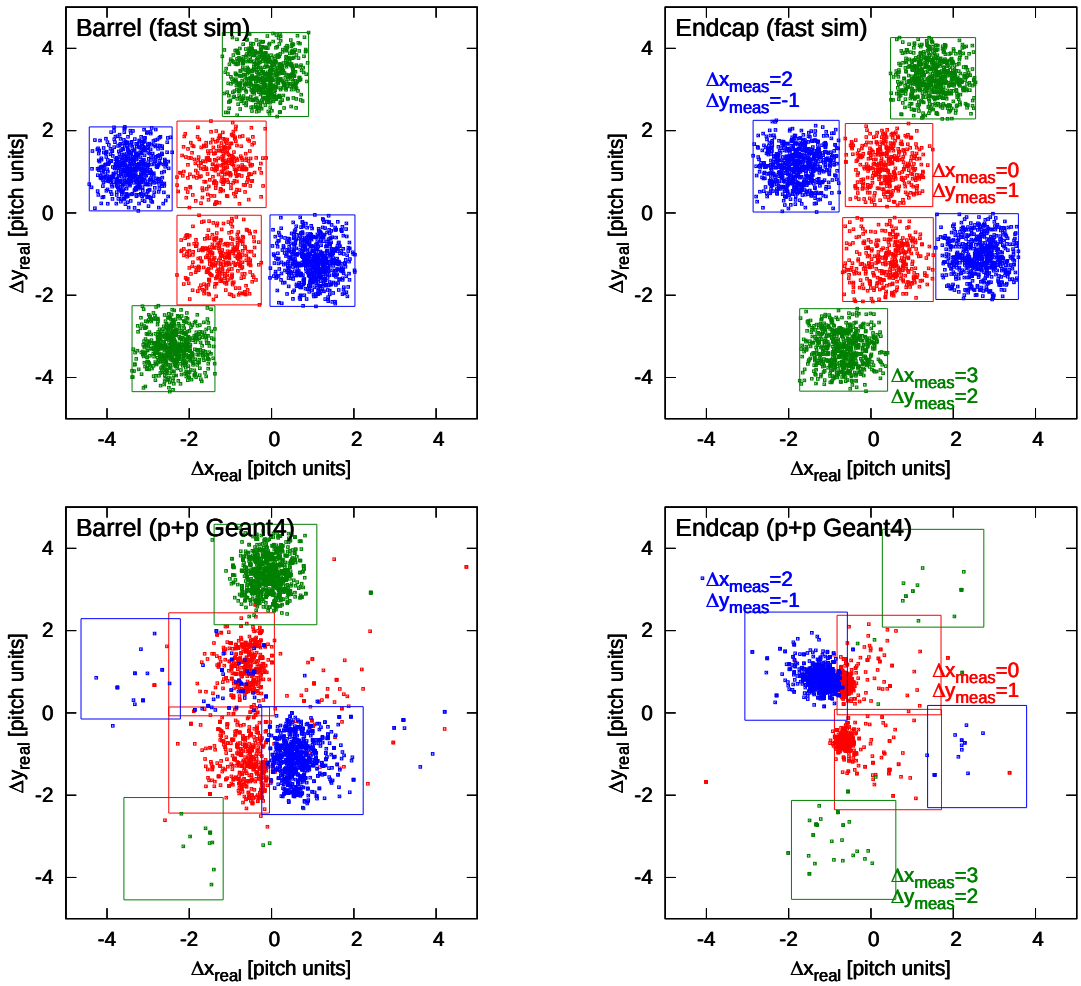


Figure 6: Distribution of the planar distances of exit and entry points, movements $(\Delta x_{real}, \Delta y_{real})$, for several measured envelopes $(\Delta x_{meas}, \Delta y_{meas})$, both in pitch units. Entries and ranges from fast calculation (fast sim) are shown for both barrel and endcap layers at the top. Entries and ranges (widened by 0.2 units) from fully simulated data (p+p Geant4) are shown at the bottom.

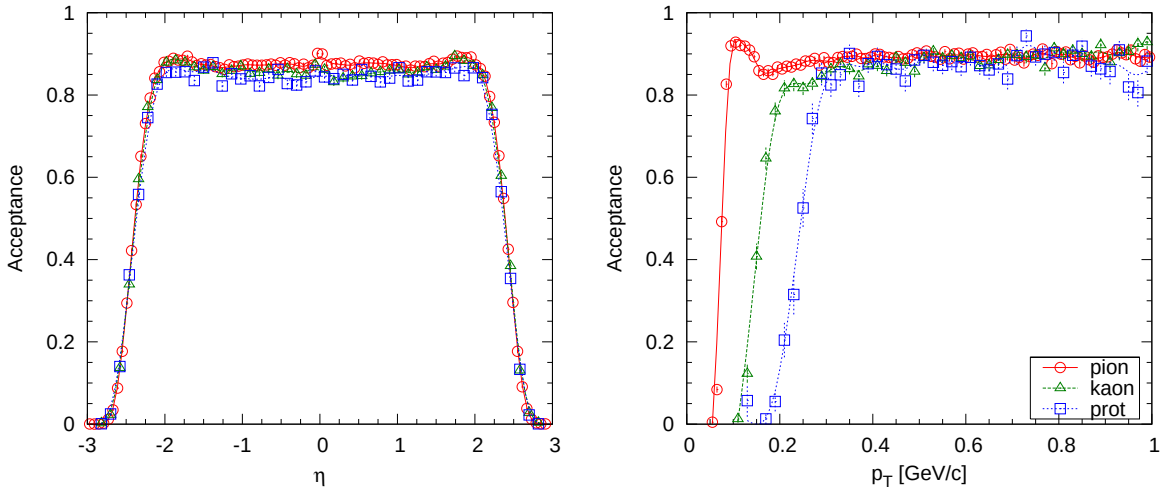


Figure 7: Acceptance as a function of $\eta$ (left) and as a function of $p_T$ (right, if the track is in the range $|\eta| < 1$). Values are given separately for pions, kaons and protons.

# 4 Results

Data sets with several settings have been prepared in order to properly demonstrate the different aspects of low $p_T$ reconstruction. They include:

- straight line vs helix: reconstruction with standard or with modified hit triplet finding
- benefits from cluster shape information: reconstruction with or without checking the angle of incidence
- luminosity and multiplicity: single minimum bias p+p events; minimum bias p+p events with low and high luminosity pile-up; single Pb+Pb events

These studies are based on 25 000 single minimum bias p+p events (Pythia generator), reconstructed with modified hit triplet finding using the standard settings (`originRadius` = 0.2 cm; `originHalfLength` = 15 cm; `originZPos` = 0 cm), but much lower minimal $p_T$ (`ptMin` = 0.075 GeV/$c$). Lines in the plots are drawn to guide the eye.

Simulated and reconstructed tracks can be compared to each other by associating their hits using spatial distances. A simulated track is reconstructed if each hit of a reconstructed track is associated to hits of the simulated track. A reconstructed track is partially matched to a simulated one if at least one, but not all of its hits are associated. A reconstructed track is fully matched if all of its hits are associated. With these notions the following properties can be defined:

- Acceptance: ratio of reconstructible to all simulated tracks. A charged particle is reconstructible if its vertex is in the cylinder of origin and if it has hits in at least three different groups of pixel layers (first, second and third barrel; closer and farther endcap).
- Efficiency: ratio of reconstructed to accepted tracks. This is the fraction of reconstructible tracks which are indeed found.
- Multiple counting: fraction of such simulated tracks which are reconstructed more than once, in other words they have more than one full match. They are mostly loopers.
- Fake rate: fraction of reconstructed tracks which are at most partially, but not fully matched to any of the simulated tracks. They are from combinatorial background.

## 4.1 Acceptance

The acceptance of the pixel detector is limited both in $\eta$ and $p_T$. While the former is evident, the latter can be illustrated by the fact that a charged primary particle can reach the third pixel barrel only if its $p_T > 0.003 \cdot B \cdot$

Table 1: Average acceptance and efficiency values in the plateau ranges $|\eta| < 1$ and $p_T > 0.5$ GeV/$c$ are shown for pions, kaons and protons. The rounded $p_T$ values where the acceptance or efficiency is at 50% or reaches the plateau are also given, in GeV/$c$ units.

| | Acceptance | | | | Efficiency | | | |
|---|---|---|---|---|---|---|---|---|
| | average | | 50% | plateau | average | | 50% | plateau |
| | $\|\eta\| < 1$ | $p_T > 0.5$ | reached at $p_T$ of | | $\|\eta\| < 1$ | $p_T > 0.5$ | reached at $p_T$ of | |
| pion | 0.88 | 0.90 | 0.08 | 0.1 | 0.90 | 0.94 | 0.10 | 0.2 |
| kaon | 0.85 | 0.90 | 0.16 | 0.2 | 0.90 | 0.94 | 0.18 | 0.3 |
| proton | 0.84 | 0.88 | 0.24 | 0.3 | 0.86 | 0.92 | 0.27 | 0.4 |

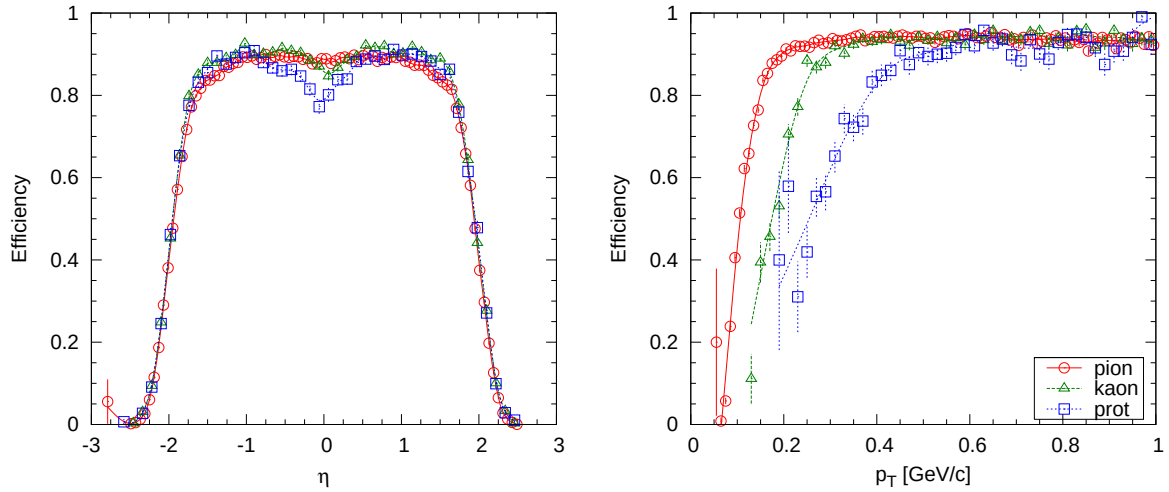


Figure 8: Efficiency as a function of $\eta$ (left) and as a function of $p_T$ (right, if the track is in the range $|\eta| < 1$). The values are given separately for pions, kaons and protons.

$R_3/2 \approx 60$ MeV/$c$ (with $B = 4$ T and $R_3 \approx 10$ cm). In reality higher momentum is needed because the particle loses energy (and momentum) in the beam-pipe, in the crossed pixel layers and support. The specific energy loss is function of $\beta\gamma = p/m$ of the particle, thus for the same momentum it is different for particles with different mass. Hence the protons and kaons are less accepted than pions, namely they have smaller range. The acceptance is slightly influenced by the multiple scattering which is again bigger for higher mass particles.

The acceptance for pions, kaons and protons as a function of $\eta$ and $p_T$ is shown in Fig. 7. It is closely flat in the range $|\eta| < 2$ for all particle types with average values 0.88, 0.85 and 0.84 (see Table 1). It rises sharply with $p_T$ and reaches a plateau at 0.1, 0.2 and 0.3 GeV/$c$ for pions, kaons and protons, respectively. The pixel detector can be used for charged particle tracking with essentially flat acceptance above these $p_T$ values.

## 4.2 Efficiency

The efficiency of the reconstruction for pions, kaons and protons as a function of $\eta$ and $p_T$ is shown in Fig. 8. It is closely flat in the range $|\eta| < 1.5$ with the exception of protons. The average values are 0.90, 0.90 and 0.86 (see Table 1). The acceptance rises sharply with $p_T$ and reaches a plateau at 0.2, 0.3 and 0.4 GeV/$c$ for pions, kaons and protons, respectively. The pixel detector can be used for charged particle tracking with essentially flat acceptance above these $p_T$ values.

## 4.3 Multiple counting

The fraction of multiply counted tracks as a function of $\eta$ and $p_T$ is shown in Fig. 9. It is below 1% near $\eta = 0$, but goes quickly to zero for $|\eta| > 0.5$. Some fraction appears at very low $p_T$ but it is already at the permille level for $p_T > 0.2$ GeV/$c$.

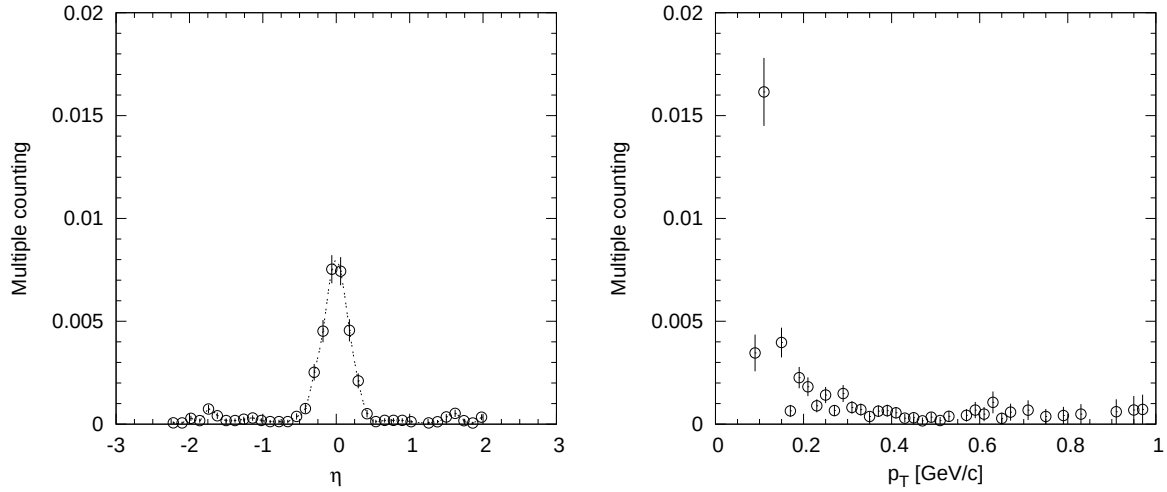


Figure 9: Fraction of multiple counted tracks as a function of $\eta$ (left) and as a function of $p_T$ (right, if the track is in the range $|\eta| < 1$).

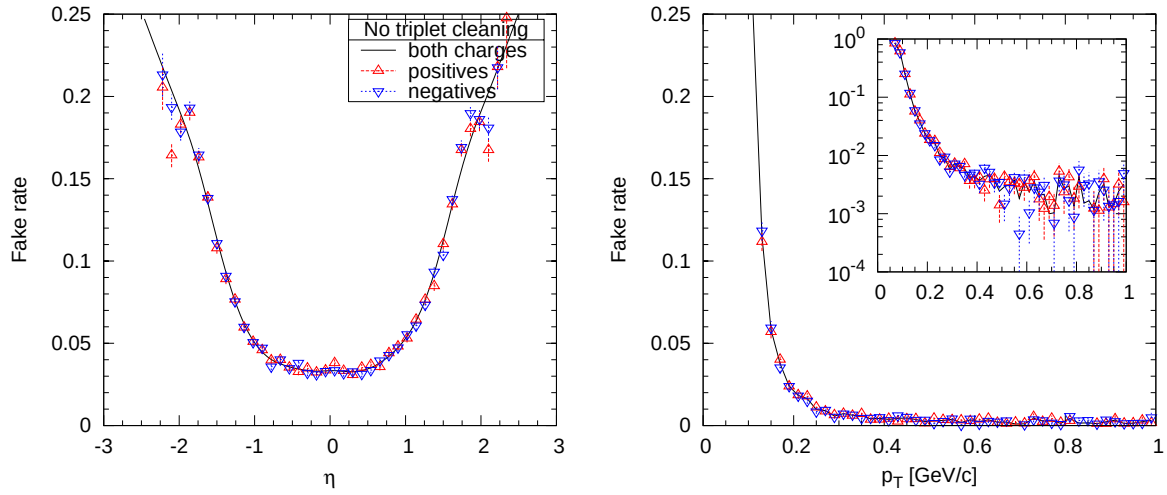


Figure 10: Fake rate without triplet cleaning as a function of $\eta$ (left) and as a function of $p_T$ (right, if the track is in the range $|\eta| < 1$). Values for both charges, positives and negatives are shown separately. The insert on the right shows the $p_T$ dependence with logarithmic vertical scale.

## 4.4 Fake rate

The fake rate as a function of $\eta$ and $p_T$, for particles of both charges, is shown without and with triplet cleaning in Fig. 10 and Fig. 11, respectively. Without cleaning the fake rate reaches 20% at $|\eta| = 2$, but even at $\eta = 0$ it stays close to 4%. With cleaning these numbers go down to about 2% and 0.5%, respectively, which is a reduction by factor 10. In the range $|\eta| < 1$ the fake rate falls steeply with increasing $p_T$. It is about 4% at 0.1 GeV/$c$ and goes below 1% at 0.16 GeV/$c$, staying at the permille level for higher $p_T$.

The shape of the pixel clusters is different for positive and negative particles of same $p_T$. The Lorentz-shift makes the clusters of the positives narrower, while those of the negatives are widened. This asymmetry is reflected in the effectiveness of the compatibility check with the angle of incidence (see Section 3), which difference propagates to the fake rate distribution. While there is no charge dependence in the no cleaning case (Fig. 10), there are half as much negative fakes as positives when cleaning is used. (The fake rate for negatives at $\eta = 0$ is about 0.3%.) In this sense the pixel detector performs better for negative particles.

## 4.5 Resolutions

The bias and resolution of the reconstructed $\eta$ and $p_T$ can be studied as a function of the simulated quantities (see plots in Fig. 12). The reconstructed $\eta$ is practically bias free with resolution in the range of 0.005 - 0.01. It is governed by multiple scattering which is inversely proportional to the total momentum. This explains why the

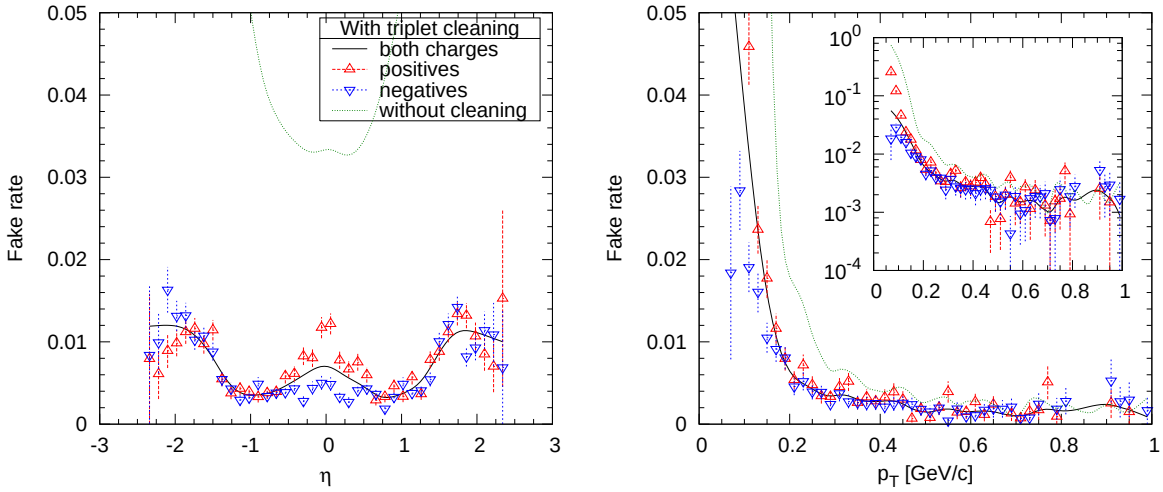


Figure 11: Fake rate with triplet cleaning as a function of $\eta$ (left) and as a function of $p_T$ (right, if the track is in the range $|\eta| < 1$). Values for both charges, positives and negatives are show separately. For comparison the result without triplet cleaning is plotted as well. Note the different vertical scale with respect to Fig. 10.

pions with lowest average momentum have the worst resolution. The reconstructed $p_T$ is generally smaller than the simulated one, the ratio of reconstructed to simulated $p_T$ converges to 0.98 for higher $p_T$ particles. This bias is probably a feature of track reconstruction. It originates from the uncertainty of hit position reconstruction which on average could push the radius of the projected circle to smaller values. At the same time the bias is larger for lower $p_T$ and for heavier particles. This observation can be readily understood, being due to the energy loss of the particle which increases with decreasing momentum and scales with $p/m$ of the particle. In case of protons a correction of about 10% needed at $p_T = 0.2$ GeV/$c$. The energy straggling is reflected in the relative resolution of $p_T$ that shows a behaviour similar to that of the bias. The relative resolution for pions and kaons converges to the value of 5.5%.

## 4.6 Performance at various conditions

The performance of low $p_T$ reconstruction was studied under several running conditions.

- Minimum bias p+p events with pile-up

  These studies are based on 25 000 minimum bias p+p events (Pythia generator). The events have been grouped according to Poissonian distribution in order to study the effect of pile-up at low-luminosity ($2 \cdot 10^{33}\mathrm{cm}^{-2}\mathrm{s}^{-1}$, 5 events per bunch-crossing on average) and at high-luminosity ($10^{34}\mathrm{cm}^{-2}\mathrm{s}^{-1}$, 25 events per bunch-crossing on average). Only in-time pile-up was considered.

- Central Pb+Pb events

  These studies are based on 25 central Pb+Pb events with two multiplicity settings (Hydjet generator with `NETA` = 30 000 called "central" and `NETA` = 15 000 called "medium"). In case of heavy ion running low intensity is expected, thus only a single event was simulated in the detector without pile-up. The multiplicity is very high: tens of thousands of charged particles are created in a central Pb+Pb collision. The primary vertex of the event was determined first with good precision using high $p_T$ tracks. With this knowledge, in a second turn, the cylinder of origin was centered on this vertex (`originZPos`) with a small half-length of `originHalfLength` = 0.1 cm. In order to further reduce the fake rate the radius of the cylinder of origin was reduced to `originRadius` = 0.1 cm. The reconstruction could be speeded up by increasing the low $p_T$ cut to `ptMin` = 0.175 GeV/$c$.

The comparison of reconstruction efficiency as a function of $\eta$ and $p_T$ is shown in Fig. 13. For Pb+Pb collisions the efficiency is generally below the p+p value in $p_T$ by about 5%.

The fake rate as a function of $\eta$ and $p_T$ is shown in Fig. 14. At $\eta = 0$ it is about 3% for low-luminosity and about 15% for high-luminosity p+p pile-up, while the central Pb+Pb value is at 13% and the medium Pb+Pb value is at 7%. The best performance for p+p events is reached at $|\eta| \approx 1$ where low-luminosity gives about 1% and the high-luminosity has about 5% fakes. The fake rate falls steeply with increasing $p_T$. At $p_T = 0.2$ GeV/$c$ it is about

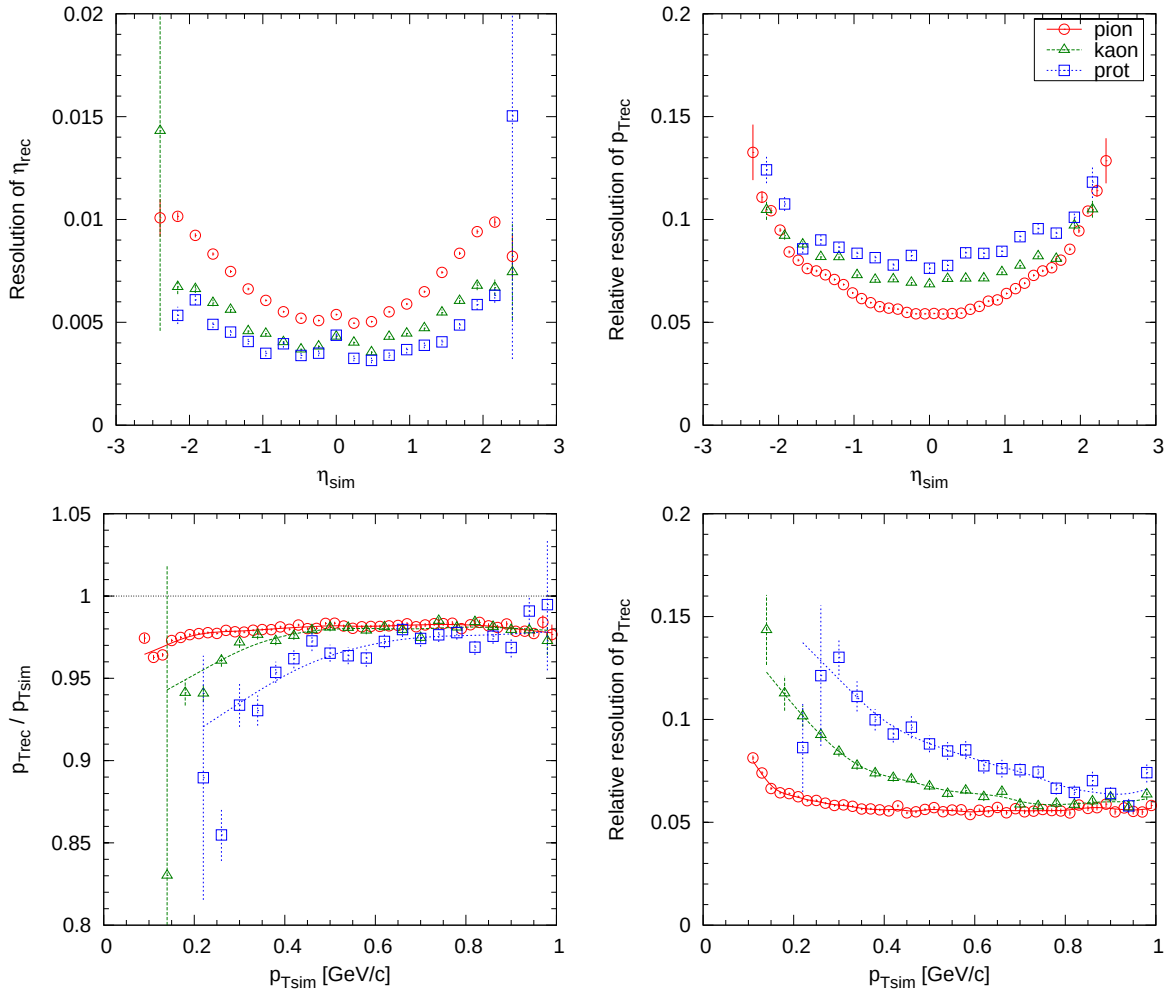


Figure 12: Resolution of track parameters. Upper left: resolution of reconstructed $\eta$ as a function of the simulated one. Lower left: ratio of reconstructed to simulated $p_T$ as a function of the simulated one, bias. Upper right and lower right: relative resolution of reconstructed $p_T$ as a function of simulated $\eta$ and $p_T$. The dependences on $p_T$ are only given in the range $|\eta| < 1$.

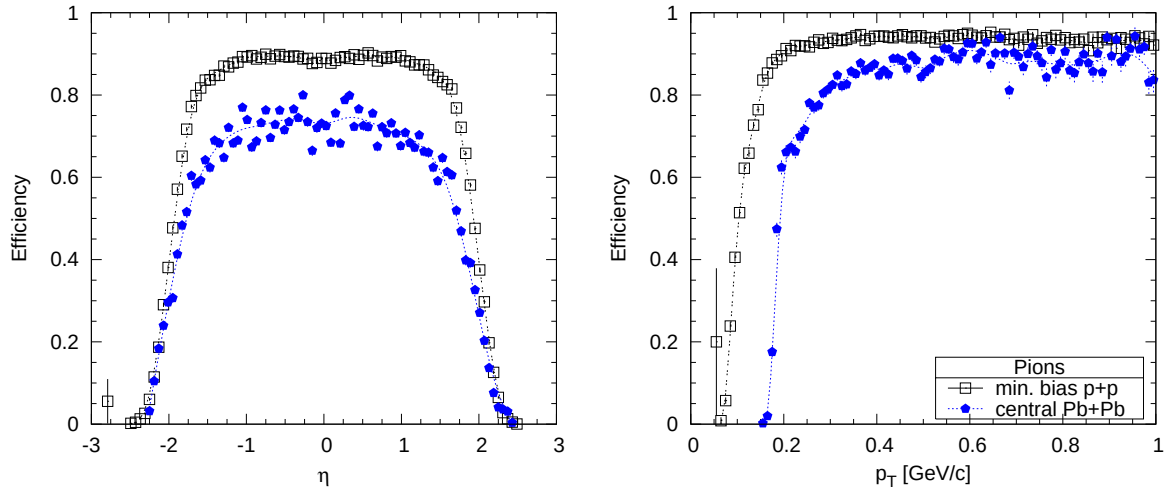


Figure 13: Comparison of pion reconstruction efficiency as a function of $\eta$ (left) and as a function of $p_T$ (right, if the track is in the range $|\eta| < 1$). Values for minimum bias p+p events are shown together with results from central Pb+Pb collisions.

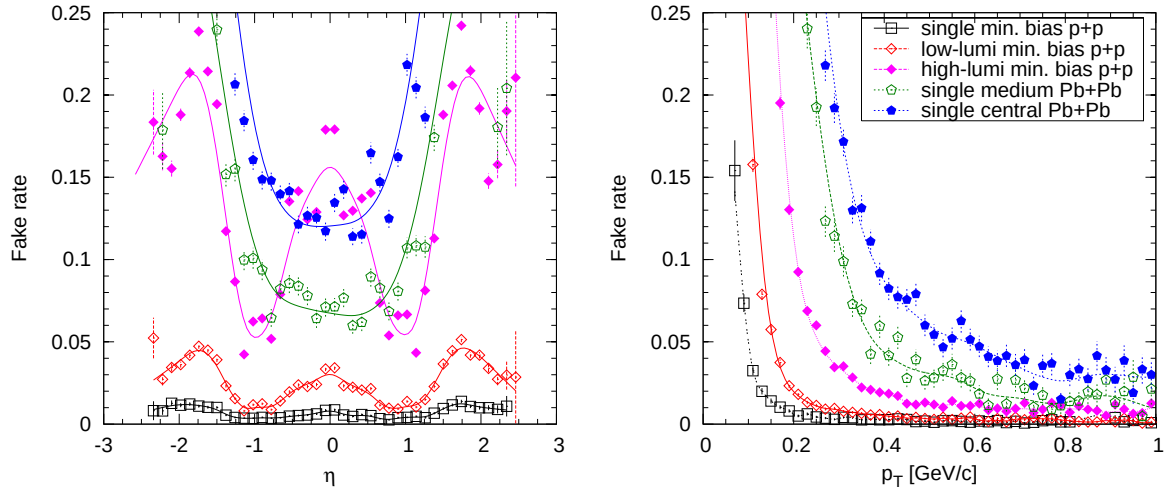


Figure 14: Fake rate as a function of $\eta$ (left) and as a function of $p_T$ (right, if the track is in the range $|\eta| < 1$). Values for single, low-luminosity and high luminosity minimum bias p+p events are shown together with results from central and medium Pb+Pb collisions.

2% for low-luminosity and about 10% for high-luminosity p+p pile-up. In case of central (medium) Pb+Pb the rate goes below 10% (5%) if $p_T > 0.4$ GeV/$c$. In case of p+p collisions the fake rate is roughly proportional to the luminosity.

The low $p_T$ reconstruction could benefit from lower magnetic field in the tracker volume (e.g. 1 T or 2 T instead of the standard 4 T) by putting particles on helices with larger radii. At the same time the acceptance is largely influenced by energy loss and multiple scattering which would stay the same even with lowered field.

# 5 Further developments

This note dealt with pixel hits only for reasons already mentioned in the introduction. Of course even low $p_T$ particles leave a lot of hits in the strip detector as well. The use of the pixel triplets can give a good starting point for global seeding in the strip part of the tracker. Strips could be used for tracking (low multiplicity p+p) or for veto (high multiplicity A+A). This trivial extension should improve momentum resolution for higher $p_T$ particles where the bend of the track is not sufficiently determined from the small volume of the pixel detector. The inclusion of strip hits should also reduce the fake rate, though those tracks where the fake rate is problematic (some 100 MeV/$c$) usually have no or few hits in the strip detector. Strip hits could also be checked for cluster shape.

Cuts and certain parameters can be optimised further, mostly for the sake of fake rate reduction in the very low $p_T$

region. For example, the choice of the cylinder of origin, its parameters, can be set differently for different sort of physics needs. The optimisation has a price: there is an interplay between efficiency and fake rate, reduction of one will increase the other.

As it was demonstrated in Section 4.6, the reconstruction of very high multiplicity Pb+Pb events can be substantially improved by determining the position of the primary vertex in advance, with help of high $p_T$ tracks. The same idea may work for high luminosity p+p events. Having found the primary vertices, in a second turn the cylinders of origins can be restricted to the proximity of those.

The specific energy loss of a charged particle is coupled to its momentum if the mass of the particle is known (Bethe-Bloch curve). In principle this information could be used for cleaning hit triplets further, by looking at the compatibility of their energy deposits with each other and with the momentum of the corresponding track. However, this type of check would definitely introduce strong bias and it was not considered further.

Although neutral particles do not deposit energy in the pixels, they can be detected via their charged decay or conversion to electron-positron pairs. By increasing the radius of origin to about 3 cm, not only charged primaries but also many secondaries are reconstructible. The combination of the resulting helices enables the reconstruction of low $p_T$ short-lived weakly-decaying particles (V0s: $\mathrm{K}^0_\mathrm{S}$, $\Lambda$ and $\overline{\Lambda}$) decaying before the first pixel barrel [4]. Low $p_T$ photons converting in the beam-pipe or in the first pixel barrel are detectable as well.

# 6 Conclusions

With modified hit triplet finding the pixel detector can be employed for the reconstruction of low $p_T$ charged particles. The acceptance of the method extends down to 0.1, 0.2 and 0.3 GeV/$c$ in $p_T$ for pions, kaons and protons, respectively. The fake rate can be greatly reduced with help of information present in the shape of the pixel cluster. Acceptance and efficiency of 80-90% can be achieved, with $p_T$ resolution of 5.5% in the central region. The fake rate for single, low-luminosity and high-luminosity p+p collisions is smaller than 2% above $p_T$ values of 0.13, 0.2 and 0.35 GeV/$c$. In case of central (medium) Pb+Pb events the fake rate goes below 10% (5%) for $p_T > 0.4$ GeV/$c$.

In summary the CMS detector is able to provide good quality data on spectra and yields of charged particles, thus contributing to the soft hadronic physics program at the LHC.

# Acknowledgement

The author wishes to thank to Sándor Hegyi, András László, Christof Roland, Gábor Veres, Dániel Barna and other members of the Heavy Ions, Tracker/b-$\tau$ and MB/UE groups for helpful discussions. This work was supported by the Hungarian Scientific Research Fund (T 048898).

# References

[1] J. P. Revol [ALICE Collaboration], *"Low-$P_T$ Proton-Proton Physics at Low Luminosity at LHC"*, Eur. Phys. J. directC **4S1** (2002) 14 [Pramana **60** (2003) 795].

[2] Christof Roland, *"Track Reconstruction in Heavy Ion Events using the CMS Tracker"*, **CMS Note 2006/031**.

[3] S. Cucciarelli, M. Konecki, D. Kotliński and T. Todorov, *"Track reconstruction, primary vertex finding and seed generation with the Pixel Detector"*, **CMS Note 2006/026**.

[4] Ferenc Siklér, *"Reconstruction of V0s and photon conversions with the pixel detector"*, **CMS Note AN-2006/101**.

# A Some geometry

This appendix shows the construction of the limiting circles and the calculation of the allowed ranges for the third hits. Some notations relevant to the discussion are given in Table 2.

## A.1 Limiting circles

The situation is substantially simplified by looking at the projection of the geometrical objects on the transverse plane: helices and cylinders will be transformed to circles. The projection of the cylinder of origin is a circle $c_0$ with center $O$ and radius $r_0$. The projection of the cylinder of the hypothetical third barrel layer is a circle $c_3$ with center $O$ and radius $r_3$. With a given $c_0$, $p_{T,min}$, $c_3$ and a point pair $P_1$ and $P_2$, each requirement ("origin", "minimum", "third", see Section 2) defines a region of allowed track trajectories. Each region is enclosed by a pair of so called limiting circles, projection of extreme trajectories. The limiting circles pass through both $P_1$ and $P_2$ and they are of two types:

- touching limiting circle: they touch the circles $c_0$ (or $c_3$)
- minimal limiting circle: they have minimal radius corresponding to $p_{T,min}$

The limiting circles can be found more easily using inversion. An inversion with center $P$ and radius $k$ has the following properties:

- it inverts a point on the inversion circle $(P, k)$ into itself
- it inverts a circle $c(C, r)$ which does not pass through $P$ into another circle $c'(C', r')$ with center $C' = P + s(C - P)$ and radius $r' = |s|r$, where $s = k^2/(CP^2 - r^2)$
- it inverts a point $C$ into another point $C' = P + s(C - P)$, where $s = k^2/CP^2$
- it inverts a circle which passes through $P$ into a line drawn through the two intersections of the circle and the inversion circle

In this concrete case the center of the inversion circle is chosen to be $P_1$ and its radius is $k = P_1P_2$. The limiting circles passing through both $P_1$ and $P_2$ are inverted into lines passing though $P_2$.

**Touching circles.** The inverse of circle $c_0(O, r_0)$ is another circle $c'_0(O'_0, r'_0)$. Two lines can be drawn from $P_2$ which touch $c'_0$ (see Fig. 15). They are the inverses of the limiting circles. The angle $\chi_0$ between these lines containing $O'_0$ is

$$\sin\frac{\chi_0}{2} = \frac{r'_0}{P_2O'_0} \qquad\qquad \chi_0 = \arccos\left(1 - \frac{2r'^2_0}{P_2O'^2_0}\right) \tag{2}$$

The bisector of this angle is in the direction $\alpha_0 = \arg(P_2\vec{O}'_0)$. The corresponding angle for circle $c_3(O, r_3)$ is obtained in a similar way (see Fig. 16).

Table 2: Some notations relevant to the geometrical discussion. The circle $c_3$ is used only if $P_3$ is searched on a hypothetical barrel layer.

| Notation | Meaning |
|---|---|
| $O$ | position of the beam-line |
| $P_1$ | inner hit of the pair, center of the inversion |
| $P_2$ | outer hit of the pair |
| $P_3$ | hypothetical third hit |
| $k$ | radius of the inversion circle, $P_1P_2$ |
| $c_0$ | circle of origin, with center $O$ and radius $r_0$ |
| $r_m$ | radius of the minimal circle corresponding to $p_{T,min}$ |
| $c_3$ | circle on which $P_3$ may lie, with center $O$ and radius $r_3$ |
| $\alpha$ | direction of the angle bisector with vertex $P_2$ |
| $\chi$ | opening of the angle with vertex $P_2$ |

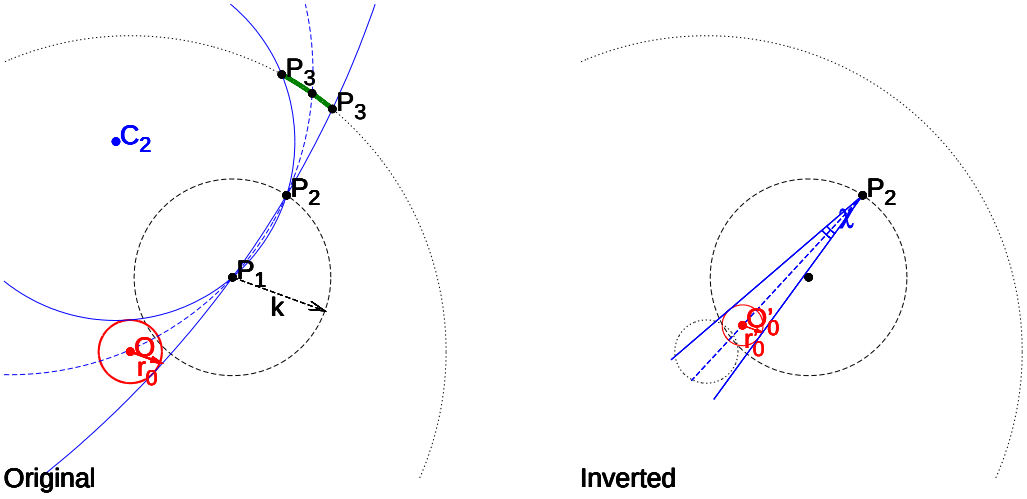


Figure 15: Determination of the limiting circles (solid blue) touching the circle of origin $c_0(O, r_0)$ (solid red). The members of the pair are $P_1$ and $P_2$. The problem is solved by inversion with center $P_1$ and radius $k = P_1P_2$. The inverted objects are shown on the right. The inverse of $P_2$ is itself. $c_0$ is inverted to another circle $c'_0(O'_0, r'_0)$. The limiting circles with centers $C_1$ (not in the figure) and $C_2$ are inverted to lines passing though $P_2$. These lines are tangent to $c'_0$. The central circle (dashed blue) is inverted to the bisector of angle $\chi$. If the third hit is searched on a circle (third barrel layer) the limiting circles cut out an arc $P_3 - P_3$ (thick green) where the candidates may be located.

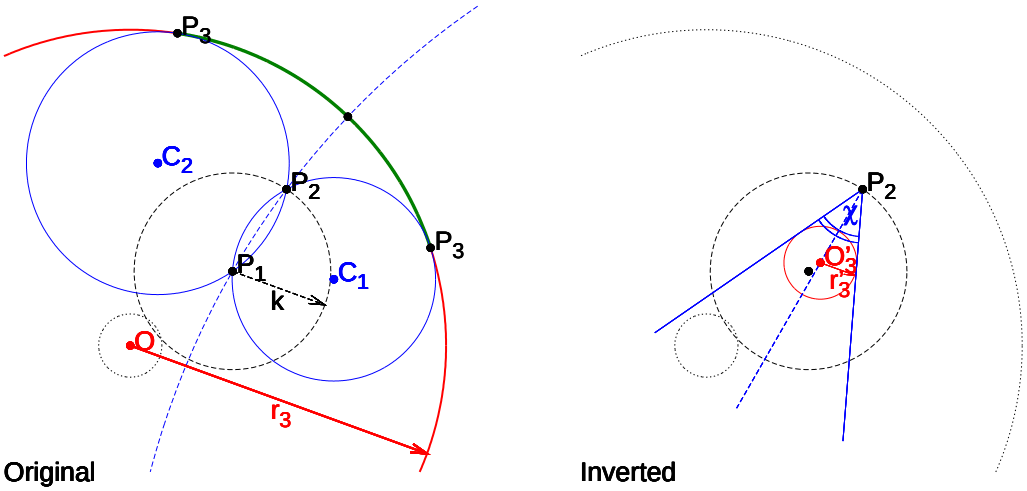


Figure 16: Determination of the limiting circles (solid blue) touching the circle $c_3(O, r_3)$ (solid red) which is the projection of a hypothetical third barrel layer. The members of the pair are $P_1$ and $P_2$. The problem is solved by inversion with center $P_1$ and radius $k = P_1P_2$. The inverted objects are shown on the right. The inverse of $P_2$ is itself. $c_3$ is inverted to another circle $c'_3(O'_3, r'_3)$. The limiting circles with centers $C_1$ and $C_2$ are inverted to lines passing though $P_2$. These lines are tangent to $c'_3$. The central circle (dashed blue) is inverted to the bisector of angle $\chi$. The limiting circles cut out an arc $P_3 - P_3$ (thick green) where the candidates may be located.

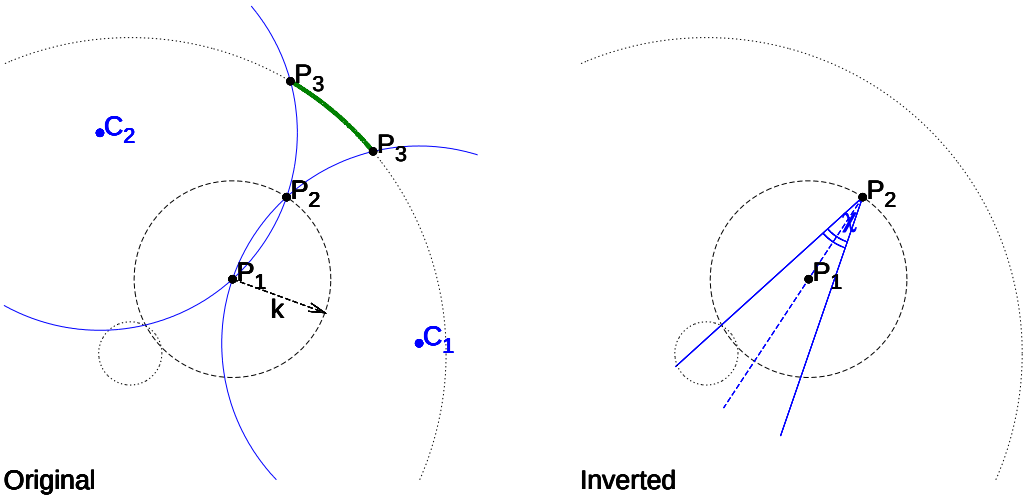


Figure 17: Determination of the minimal circles (solid blue) having minimal radius corresponding to $p_{T,min}$. The members of the pair are $P_1$ and $P_2$. The problem is solved by inversion with center $P_1$ and radius $k = P_1P_2$. The inverted objects are shown on the right. The inverse of $P_2$ is itself. The minimal circles with centers $C_1$ and $C_2$ are inverted to lines passing though $P_2$. The central line drawn through both $P_1$ and $P_2$ is inverted to the bisector (dashed blue) of angle $\chi$. If the third hit is searched on a circle (third barrel layer) the minimal circles cut out an arc $P_3 - P_3$ (thick green) where the candidates may be located.

**Minimal circles.** The inverses of the minimal circles are lines passing through $P_2$ (see Fig. 17). The angle $\chi_m$ between these lines containing $P_1$

$$\sin\frac{\chi_m}{2} = \frac{k}{2r_m} \qquad \chi_m = \arccos\left(1 - \frac{k^2}{2r_m^2}\right) \tag{3}$$

The bisector of this angle is in the direction $\alpha_m = \arg(P_2\vec{P}_1)$.

In the end each pair of limiting circles is transformed into an angle described by bisector $\alpha$ and opening $\chi$ with a common vertex $P_2$. The common part $(\alpha_c, \chi_c)$ of these angles is given by their intersection $(\alpha_0, \chi_0) \bigcap (\alpha_m, \chi_m)$ or $(\alpha_0, \chi_0) \bigcap (\alpha_m, \chi_m) \bigcap (\alpha_3, \chi_3)$. If the result is not empty, it represents the region of allowed trajectories in the inverted space which fulfil all the requirements.

Three unit vectors $\vec{v_-}$, $\vec{v_0}$ and $\vec{v_+}$ are formed belonging to three special trajectories.

- $\arg(\vec{v_-}) = \alpha_c - \chi_c/2$, "lower" leg of the common angle, inverse of one of the common limiting circles
- $\arg(\vec{v_0}) = \alpha_c$, bisector of the common angle, inverse of the central circle
- $\arg(\vec{v_+}) = \alpha_c + \chi_c/2$, "upper" leg of the common angle, inverse of the another common limiting circle

The lines belonging to these vectors are transformed back to the original space giving the three special circles. The center $C$ of such a circle is be determined in the following way. Let $A$ denote the antipode of $P_1$ on the circle. The inverse of this point is at $A' = P_2 - \vec{v}[\vec{v}(P_2 - P_1)]$. The center of the common limiting circle is at $C = \frac{P_1+A}{2}$. Any circle that passes through both $P_1$ and $P_2$ and located in the region limited by the common limiting circles fulfils all the requirements.

## A.2 Allowed ranges

With help of the $z$ coordinates of points $P_1$ and $P_2$, any allowed circle can be transformed back to a helix. The candidates for third hit are located on a layer (Fig. 18). The thrusts of allowed helices on the surface of that layer form a curve. It is not necessarily a line, but already well approximated by a parabola in proper coordinates: $(\phi, z)$ for barrel and $(\phi, r)$ for endcap. A parabola is be defined from three points, hence three special trajectories are needed. The next task is to calculate the thrust of the limiting helices and the central helix on the layer.

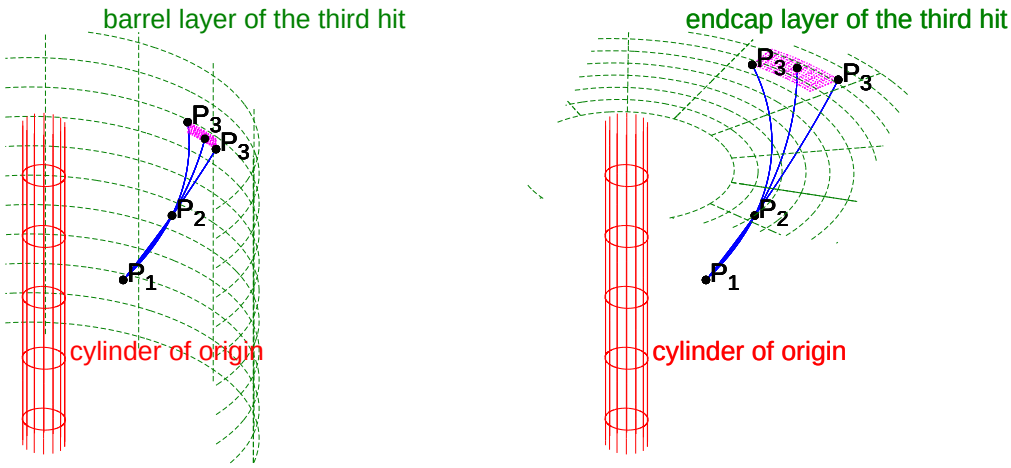


Figure 18: Determination of the possible range of the third hit candidates in case of a barrel layer (left) and an endcap layer (right), shown in three dimensions. The cylinder of origin (red) and the layers (green) are indicated. The members of the pair are $P_1$ and $P_2$. Curves of the two extreme trajectories (solid blue) and the central trajectory (dashed blue) are drawn together with the three thrust points $P_3$. These points define a parabola whose rectangular envelope is given (magenta grid).

**Barrel layer.** The inverse of $c_3(O, r_3)$ is another circle $c_3'(O_3', r_3')$. The intersections of the special circles and $c_3$ have to be found first. With help of the corresponding unit vector $\vec{v}$ the inverse of the intersection $P_3(\vec{v})$ is at

$$P_3' = P_2 + \vec{v}\left[\vec{P_2O_3'}\cdot\vec{v} - \sqrt{r_3'^2 + (\vec{P_2O_3'}\cdot\vec{v})^2 - P_2O_3'^2}\right] \tag{4}$$

The $\phi$ coordinate is given by $\arg\vec{OP_3}$. Due to the nature of the helix, there is a linear relationship between the azimuthal angle with respect to the center of the circle and the $z$ coordinate. This way the $z$ coordinate also be calculable. In the end there are three pairs of $(\phi, z)$ values for each special helices belonging to unit vectors $\vec{v_-}$, $\vec{v_0}$ and $\vec{v_+}$.

**Endcap layer.** A hypothetical endcap layer is described by its coordinate $z_3$. Due to the linear relationship mentioned in the previous paragraph, the angle $\angle P_2CP_3$ is calculated. The position of $P_3$ is obtained by moving along the helix with this angle. In the end there are three pairs of $(\phi, r)$ values for each special helices belonging unit vectors $\vec{v_-}$, $\vec{v_0}$ and $\vec{v_+}$.

The coordinates of the three thrust points can be readily used for parabola fit. The hit cache providing third hit candidates expects a rectangular area in $(\phi, z/r)$ coordinates. In order to match that, a rectangular envelope of the corresponding part of parabola is calculated (for details see Fig. 19).

# B Event gallery

Plots of reconstructed single minimum bias p+p events are shown in Fig. 20.

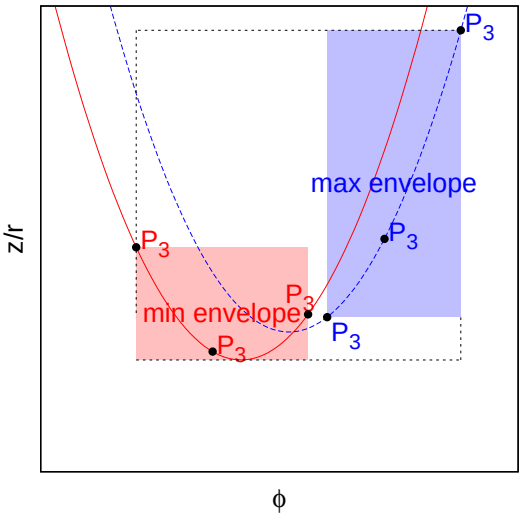


Figure 19: Determination of the rectangular envelopes. The third hits $P_3$ are thrust points of the three special trajectories on the hypothetical layer. These hits determine a parabola whose envelope can be calculated. There are two envelopes, one belonging to the minimal range of the layers(”min envelope”, solid red) the other to the maximal range of the layers (”max envelope”, dashed blue). The range means either radius (barrel) or $z$ coordinate (endcap). The final common envelope is also drawn (dotted black).

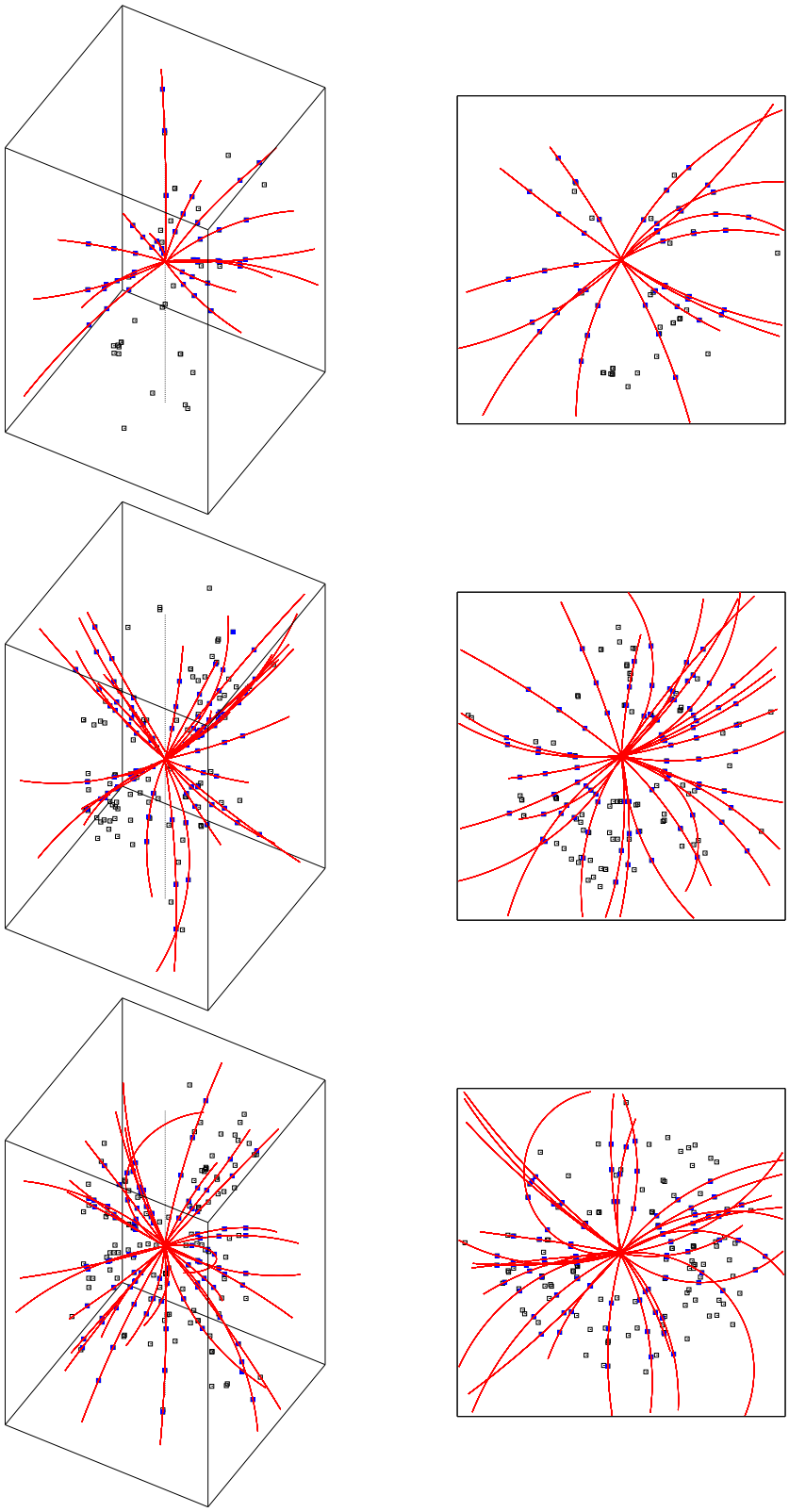

Figure 20: Plots of reconstructed single minimum bias p+p events. Hits are shown by open black boxes. Those hits which belong to a reconstructed track are indicated by filled blue boxes. The helices of the reconstructed trajectories are drawn with solid red lines. Both the three dimensional view and its planar projection are shown.